

Pushing spectral siren cosmology into the third-generation era: a blinded mock data challenge

Matteo Tagliazucchi^{1,2,3} *, Michele Moresco^{1,2} , Alessandro Agapito⁴ , Michele Mancarella⁴ , Sarah Ferraiuolo^{5,6,7} , Simone Mastrogiovanni⁵ , Nicola Borghi^{1,2,3} , Francesco Pannarale^{5,6} , Daniele Bonacorsi^{1,3} 

¹ Dipartimento di Fisica e Astronomia “Augusto Righi”–Università di Bologna, Viale Berti Pichat 6/2, I-40127 Bologna, Italy

² INAF - Osservatorio di Astrofisica e Scienza dello Spazio di Bologna, via Piero Gobetti 93/3, I-40129 Bologna, Italy

³ INFN - Sezione di Bologna, Viale Berti Pichat 6/2, I-40127 Bologna, Italy

⁴ Aix-Marseille Université, Université de Toulon, CNRS, CPT, Marseille, France

⁵ INFN, Sezione di Roma, Piazzale Aldo Moro 5, I-00185 Roma, Italy

⁶ “Sapienza” Università di Roma, Piazzale Aldo Moro 5, 00185 Roma, Italy

⁷ Aix Marseille Univ, CNRS/IN2P3, CPPM, Marseille, France

February 23, 2026

ABSTRACT

Gravitational wave (GW) spectral sirens offer a promising method for measuring cosmological parameters using GW data only — without relying on external redshift information such as electromagnetic counterparts or galaxy catalogs — by exploiting distributional features in the population of GW sources. The advent of third-generation detectors like the Einstein Telescope (ET) will provide catalogs three orders of magnitudes larger than current ones, raising questions about the scalability and robustness of existing inference pipelines. We present a blinded mock data challenge that tests three public pipelines with distinct numerical implementations, namely, ICAROGW, CHIMERA, and PYMCPOP-GW, on simulated ET observations containing the best $O(10^4)$ binary black hole mergers that can be observed in 1 year. We assess their computational performance, validate their agreement in a blinded setting, and forecast cosmological constraints. We find that, thanks to GPU acceleration, these pipelines can process the events expected from ET within a manageable timeframe. All pipelines recover consistent cosmological and population parameters. Assuming a flat Λ CDM model, we measure $H(z)$ at $z \sim 1.5$ with 2.4% precision, and achieve a mean precision on $H(z)$ of 2.8% across $0.7 < z < 1.8$ with a catalog of $\sim 12,000$ high-S/N events. This corresponds to joint constraints of $\sim 10\%$ on H_0 and $\sim 26\%$ on $\Omega_{m,0}$. We also identify the events that contribute mostly to constraining cosmological parameters, showing that low-distance sources near population features drive the constraining power on all cosmological parameters, while higher-distance events primarily constrain $\Omega_{m,0}$. Our results establish a validated, performance-tested framework for spectral siren cosmology in the era of third-generation GW observatories.

Key words. gravitation - gravitational waves – cosmology: observations - methods: data analysis

1. Introduction

Since the first direct detection of gravitational waves (GWs) by the LIGO-Virgo Collaboration in 2015 (Abbott et al. 2016), GW observations have opened a new observational window, providing cosmological information complementary to that of electromagnetic (EM) probes. GWs can be used as standard cosmological rulers, as they allow for a direct measurement of the luminosity distance to the source, independent of the traditional cosmic distance ladder. When combined with redshift information, they enable constraints on cosmological parameters, such as the Hubble constant (Schutz 1986; Holz & Hughes 2005; Moresco et al. 2022; Jin et al. 2026), thereby probing the expansion history of the Universe across cosmic time.

A fundamental challenge for GW-based cosmology is the degeneracy between the source redshift and the intrinsic mass scale of the binary system. Several methods have therefore been developed to infer redshift information statistically. One prominent approach is the dark-siren method, which relies on cross-correlating the GW sky localization volume with galaxy catalogs and assigning probabilistic weights to potential host galaxies (Del Pozzo 2012; Chen et al. 2018; Fishbach et al.

2019; Gray et al. 2020; Finke et al. 2021; Gray et al. 2022; Belfiglio et al. 2022; Gair et al. 2023).

In this work, we focus on the spectral siren method, which exploits features in the population distribution of GW source parameters, most notably the mass distribution, to statistically disentangle redshift and intrinsic properties across the detected population (Taylor et al. 2012; Farr 2019; Mastrogiovanni et al. 2021). This approach enables the joint inference of cosmological and population hyperparameters without relying on external redshift measurements.

Several analysis pipelines have been developed to implement this joint inference framework, including ICAROGW (Mastrogiovanni et al. 2023, 2024), gwcsmo (Gray et al. 2023), CHIMERA (Borghi et al. 2024; Tagliazucchi et al. 2025), and PYMCPOP-GW (Mancarella & Gerosa 2025). Dark and spectral siren techniques have already been applied to current LIGO–Virgo–KAGRA observations, yielding constraints on the Hubble constant (Abbott et al. 2023b, 2021a; Abac et al. 2025b) from the publicly available GWTC-4.0 catalog and its previous versions (Abbott et al. 2019, 2021b, 2023a; Abac et al. 2025d). These measurements, however, remain limited by detector sensitivity and the relatively small number of detected events.

* matteo.tagliazucchi2@unibo.it

This situation will change substantially with the advent of third-generation (3G) GW detectors. Two concepts are currently under consideration for construction in the 2030s: the Einstein Telescope (ET) in Europe (Hild et al. 2011; Punturo et al. 2010; Maggiore et al. 2020) and the Cosmic Explorer (CE) in the United States (Reitze et al. 2019; Evans et al. 2021). Their improved sensitivity and extended low-frequency coverage will enable the detection of compact binary mergers over a broad redshift range, potentially reaching the dark ages, with expected detection rates of up to millions of events over a timescale of approximately ten years (Maggiore et al. 2020; Iacovelli et al. 2022a; Branchesi et al. 2023; Abac et al. 2025a).

In this high-statistics regime, the accuracy and precision of cosmological constraints will be driven not only by detector sensitivity, but also by the behavior of inference pipelines when confronted with large and heterogeneous data sets. Key questions include how constraints scale with the number of detected events, and whether analysis pipelines remain stable and unbiased as the dimensionality and volume of the data increase. These issues involve convergence properties, sampling efficiency, and robustness to modeling assumptions. Moreover, a critical question is whether current cosmological pipelines can scale to accommodate the expected future number of detected GW events, which are projected to increase by three orders of magnitude. Notably, different spectral siren pipelines implement the hierarchical likelihood using distinct numerical strategies. Therefore, ensuring that these different numerical implementations produce consistent and unbiased results is a key aspect of validation for the 3G era.

To address these challenges, we perform a blinded mock data challenge (MDC) designed to test some of the publicly available spectral siren pipelines under realistic observational conditions expected for ET. The use of blinded analyses allows for an unbiased validation of inference pipelines and enables a controlled comparison of different implementations. This study represents a first stress test of these codes at the data volume expected from third-generation detectors, providing both a performance comparison and a forecast of the execution times required for future analyses. Moreover, this study features the first direct comparison between codes that compute the likelihood for inferring cosmological parameters from GW data in three different ways, allowing us to validate their numerical consistency and to identify potential systematic differences. Additionally, we investigate the contribution of GW events to the reconstruction of the cosmic expansion history, thereby identifying the regimes in the observed parameter space in which the constraining power of spectral sirens is strongest.

This paper is organized as follows. In Sec. 2 we introduce the statistical framework for spectral siren inference and describe the analysis pipelines employed in this study, including implementations based on ICAROGW, CHIMERA, and PYMCPop-GW. In Sec. 3, we detail the construction of the blinded mock catalogs and the design of the mock data challenge. Section 4 presents the results of the MDC, focusing on pipeline performance, convergence behavior, and cosmological constraints. We conclude in Sec. 5 with a discussion of the implications of our findings and possible future developments.

2. Framework

Constraining cosmological and population parameters Λ (such as H_0 , merger rate density, and mass distribution) from a set of GW observations $\{\mathbf{d}_i\}_{i=1}^{N_{\text{obs}}}$ is a hierarchical problem, as it requires inferring population-level parameters from the measured

detector-frame properties of individual events $\{\theta_{d,i}\}_{i=1}^{N_{\text{obs}}}$ (e.g. redshifted masses, and luminosity distance). The hierarchical likelihood of obtaining N_{obs} observations over an observing time T_{obs} in presence of selection effect is (see, e.g., Mandel et al. 2019; Vitale et al. 2020, for a detailed derivation):

$$\begin{aligned} \mathcal{L}(\{\mathbf{d}_i\}_{i=1}^{N_{\text{obs}}} | \Lambda) &\propto e^{-N_{\text{exp}}(\Lambda)} \times \\ \prod_{i=1}^{N_{\text{obs}}} T_{\text{obs}} \int d\theta_{d,i} \mathcal{L}_{\text{gw}}(\mathbf{d}_i | \theta_{d,i}) \frac{dt_i}{dt_{d,i}} \left| \frac{d\theta_i}{d\theta_{d,i}} \right| \frac{dN}{dt_i d\theta_i}(\Lambda) &\equiv \\ &\equiv e^{-N_{\text{exp}}(\Lambda)} \prod_{i=1}^{N_{\text{obs}}} T_{\text{obs}} I_i, \end{aligned} \quad (1)$$

where \mathcal{L}_{gw} is the single GW event likelihood, $\frac{dN}{dt d\theta}(\Lambda)$ is the population model describing the rate of events with source-frame parameters θ , and $\left| \frac{d\theta}{d\theta_d} \right|$ is the Jacobian computed from the source- to the detector-frame. t is the coalescing time in source-frame and t_d the corresponding detector-frame time, and the factors $\frac{dt}{dt_d}$ accounts for their conversion. The $N_{\text{exp}}(\Lambda)$ term represents the expected number of detectable sources over T_{obs} , given the population model:

$$N_{\text{exp}}(\Lambda) = T_{\text{obs}} \int d\theta_d P_{\text{det}}(\theta_d) \frac{dt}{dt_d} \left| \frac{d\theta}{d\theta_d} \right| \frac{dN}{dt d\theta}(\Lambda), \quad (2)$$

where $P_{\text{det}}(\theta_d)$ is the probability that an event with parameters θ_d is detected by the considered detector network.

In the spectral siren case, dropping the assumption that GW events of interest here originate in galaxies, the population model and the Jacobian are given by:

$$\frac{dN}{dt d\theta}(\Lambda) = R_0 \psi(z | \lambda_r) \frac{dV_c}{dz}(z | \lambda_c) p(m_1, m_2 | \lambda_m), \quad (3)$$

$$\left| \frac{d\theta}{d\theta_d} \right| = \left| \frac{\partial d_L(z | \lambda_c)}{\partial z} \right|^{-1} (1+z)^{-2}, \quad (4)$$

$$\frac{dt}{dt_d} = (1+z)^{-1}, \quad (5)$$

where R_0 is rate of sources per year and comoving volume, $\psi(z | \lambda_r)$ describes the merger rate evolution, dV_c/dz is the comoving volume element, and $p(m_1, m_2 | \lambda_m)$ is the mass distribution (see Mastrogiovanni et al. 2024, for more details). It is clear from the previous equations that the hierarchical formalism actually fits the detector-frame population rate, $\frac{dN}{dt d\theta_d}$. Population and cosmological parameters are obtained by assuming a source-frame population rate, and then propagating it in the detector frame given a cosmological model (Pierra et al. 2025). Features in the population model, such as peaks, gaps, or breaks in the mass distribution, act as cosmological rulers and add information to constrain cosmological parameters. These features, which statistically break the mass-redshift degeneracy, are those that mostly drive the constraining power in the spectral siren approach.

We now describe three codes that compute the likelihood in Eq. (1) differently. The first code, ICAROGW, calculates the likelihood using a Monte Carlo sum, as done in MGCosmoPop (Mancarella et al. 2022). CHIMERA, instead, uses a Kernel Density Estimate (KDE) approach to handle the integrals in Eq. (1), analogously to gwcsmo (Gray et al. 2023). Finally, PYMCPop-GW implements a version of Eq. (1) that is not marginalized over the event parameters.

2.1. ICAROGW implementation

In the ICAROGW pipeline, the integrals I_i in Eq. (1) are approximated using Monte Carlo integration

$$I_i = \frac{1}{N_{\text{pe}}} \sum_{k=1}^{N_{\text{pe}}} \frac{1}{\pi(\theta_{d,i}^k)} \frac{d\mathbf{t}_i^k}{d\mathbf{t}_{d,i}^k} \left| \frac{d\theta_i^k}{d\theta_{d,i}^k} \right| \frac{dN}{d\mathbf{t}_i^k d\theta_i^k}(\Lambda) \equiv \frac{1}{N_{\text{pe}}} \sum_{k=1}^{N_{\text{pe}}} n_i^k, \quad (6)$$

where we used the Bayes theorem $\mathcal{L}_{\text{gw}}(\mathbf{d}_i | \theta_{d,i}) = p_{\text{gw}}(\theta_{d,i} | \mathbf{d}_i) / \pi(\theta_{d,i})$ and $\theta_{d,i}^k$ are posterior estimate (PE) samples of the i -th event drawn from p_{gw} . The expected number of sources N_{exp} is estimated via an injection campaign: N_{inj} events are drawn from a prior π_{inj} and processed through a detection pipeline. The number of detected events N_{det} is used to approximate Eq. (2) as a Monte Carlo sum over detected events (Tiwari 2018; Abbott et al. 2021c):

$$N_{\text{exp}}(\Lambda) = \frac{1}{N_{\text{inj}}} \sum_{j=1}^{N_{\text{det}}} \frac{1}{\pi_{\text{inj}}(\theta_{d,j})} \frac{d\mathbf{t}_j}{d\mathbf{t}_{d,j}} \left| \frac{d\theta_j}{d\theta_{d,j}} \right| \frac{dN}{d\mathbf{t}_j d\theta_j}(\Lambda). \quad (7)$$

For a detailed explanation of its functionality, refer to Mastrogiovanni et al. (2024).

2.2. CHIMERA implementation

In the CHIMERA code, Eq. (2) is approximated as in the ICAROGW pipeline (see Eq. (7)), whereas the integrals I_i appearing in Eq. (1) are evaluated differently. Using Bayes' theorem and the detector-to-source-frame transformation $d\theta_{d,i} p_{\text{gw}}(\theta_{d,i} | \mathbf{d}_i) = d\theta_i p_{\text{gw}}(\theta_i(\theta_{d,i}, \lambda_c) | \mathbf{d}_i)$, the integrals I_i become

$$\begin{aligned} I_i &= R_0 \int d\theta_i \frac{p_{\text{gw}}(\theta_i(\theta_{d,i}, \lambda_c) | \mathbf{d}_i)}{\pi_{\text{gw}}(\theta_{d,i})} \times \\ & p(z_i, \hat{\Omega}_i | \Lambda) p(\tilde{\theta}_i | z_i, \hat{\Omega}_i, \Lambda) \left| \frac{d\mathbf{t}_i}{d\mathbf{t}_{d,i}} \right| \left| \frac{d\theta_i}{d\theta_{d,i}} \right| = \\ &= R_0 \int dz_i d\hat{\Omega}_i \mathcal{K}_{\text{gw}}(z_i, \hat{\Omega}_i | \mathbf{d}_i, \Lambda) p(z_i, \hat{\Omega}_i | \Lambda). \end{aligned} \quad (8)$$

Here, the source-frame population rate has been factorized into the overall normalization R_0 , a term depending on redshift z and sky-localization area $\hat{\Omega}$, and a term involving the remaining source parameters $\tilde{\theta}$. In the spectral siren case, the $\tilde{\theta}$ parameters are only binary masses (see Eq. (3)). The GW kernel $\mathcal{K}_{\text{gw}}(z_i, \hat{\Omega}_i | \mathbf{d}_i, \Lambda)$ is evaluated using a weighted KDE

$$\begin{aligned} \mathcal{K}_{\text{gw}}(z_i, \hat{\Omega}_i | \mathbf{d}_i, \Lambda) &= \int d\tilde{\theta}_i \frac{p_{\text{gw}}(\theta_i(\theta_{d,i}, \lambda_c) | \mathbf{d}_i)}{\pi_{\text{gw}}(\theta_{d,i})} \times \\ & p(\tilde{\theta}_i | z_i, \hat{\Omega}_i, \Lambda) \left| \frac{d\mathbf{t}_i}{d\mathbf{t}_{d,i}} \right| \left| \frac{d\theta_i}{d\theta_{d,i}} \right| = \\ &= \text{KDE} \left[(z_i^k, \hat{\Omega}_i^k) | w_i^k \right]. \end{aligned} \quad (9)$$

The KDE is built on the PE samples $(z_i^k, \hat{\Omega}_i^k)$ drawn from the marginalized GW distribution of the i -th event $p_{\text{gw}}(z_i, \hat{\Omega}_i | \tilde{\theta}_i, \mathbf{d}_i, \lambda_c)$, each weighted by

$$w_i^k = \frac{p(\tilde{\theta}_i^k | z_i^k, \hat{\Omega}_i^k, \Lambda) \left| \frac{d\mathbf{t}_i^k}{d\mathbf{t}_{d,i}^k} \right| \left| \frac{d\theta_i^k}{d\theta_{d,i}^k} \right|}{\pi_{\text{gw}}(\theta_{d,i}^k)}. \quad (10)$$

The KDE is then evaluated on the integration volume of the i -th event. In CHIMERA there are three different ways to efficiently build and evaluate the KDE in Eq. (9). For the spectral siren analyses presented in this work, the ‘‘single-1d’’ binned method (see Tagliacruzchi et al. 2025 for the detailed description of the algorithm) is used.

2.3. PYMCPPOP-GW implementation

The package PYMCPPOP-GW follows the strategy introduced by Mancarella & Gerosa (2025), which avoids the Monte Carlo marginalization over single-event parameters that appears in the standard implementation of Eq. (1). Instead of integrating over $\theta_{d,i}$ at each likelihood call, PYMCPPOP-GW samples the *full* hierarchical posterior in an enlarged parameter space, where the event-level parameters $\{\theta_{d,i}\}$ are treated as latent variables alongside the hyper-parameters Λ .

The key step is to consider the full hierarchical posterior on $\{\Lambda, \theta_{d,i}\}_{i=1}^{N_{\text{obs}}}$, or equivalently the likelihood

$$\begin{aligned} \mathcal{L}(\{\mathbf{d}_i\}_{i=1}^{N_{\text{obs}}} | \Lambda, \{\theta_{d,i}\}_{i=1}^{N_{\text{obs}}}) &\propto e^{-N_{\text{exp}}(\Lambda)} \times \\ \prod_{i=1}^{N_{\text{obs}}} T_{\text{obs}} \frac{p_{\text{gw}}(\theta_{d,i} | \mathbf{d}_i)}{\pi_{\text{gw}}(\theta_{d,i})} \frac{d\mathbf{t}_i}{d\mathbf{t}_{d,i}} \left| \frac{d\theta_i}{d\theta_{d,i}} \right| \frac{dN}{d\mathbf{t}_i d\theta_i}(\Lambda), \end{aligned} \quad (11)$$

and implementing $p_{\text{gw}}(\theta_{d,i} | \mathbf{d}_i)$ as an effective (data-dependent) proposal/prior for each event, while the population information enters only through the reweighting factor multiplying it in Eq. (11). Compared to ICAROGW and CHIMERA, this eliminates the per-event Monte Carlo sum over PE samples in the numerator of Eq. (1), leaving selection effects as the only Monte Carlo ingredient through $N_{\text{exp}}(\Lambda)$ (estimated from injections as in Eq. (7)), at the cost of sampling a higher-dimensional posterior. This is achieved using Hamiltonian Monte Carlo.

Since gradient-based samplers require continuous and differentiable densities, PYMCPPOP-GW replaces the discrete PE samples with a continuous approximation of p_{gw} . Following Mancarella & Gerosa (2025), the interpolation is performed in a reparameterized detector-frame space (using the detector frame chirp mass - \mathcal{M}_c^d , the mass ratio - q , and the luminosity distance - d_L , and log/unbounding transforms) to avoid sharp boundaries. The interpolator is built via a Gaussian Mixture Model, with the number of components selected by minimizing the Bayesian Information Criterion.

3. Blinded mock catalogs

To generate the mock catalogs used in this analysis, we model the population of binary black hole (BBH) sources as follows. The merger rate distribution is assumed to follow the star formation history, described by the Madau–Dickinson formula (Madau & Dickinson 2014). The mass distribution is a power-law-plus-peak (PLP) law (see Sec. C of Abac et al. 2025b, for more details). The underlying cosmological model is assumed to be flat Λ CDM. The summary of all hyperparameters considered is given in Table 1.

The fiducial parameters for this population model are drawn from the constraints for this model from the GWTC-3 catalog (Abbott et al. 2023c). The posterior distribution from which the fiducial parameters were drawn is obtained with intentionally narrower priors on the cosmological parameters (specifically, $H_0 \in [60, 80]$ km/s/Mpc and $\Omega_{\text{m},0} \in [0.2, 0.4]$) to ensure that the selected fiducial values remain physically plausible and avoid unrealistic extremes. A strict blinding procedure is then implemented: the drawn fiducial parameters, along with the computed total number of coalescences in one year given the fiducial model, are immediately sent via an automated Python script to an external collaborator for safekeeping and are subsequently deleted from the origin server to ensure the blinding in the subsequent analysis.

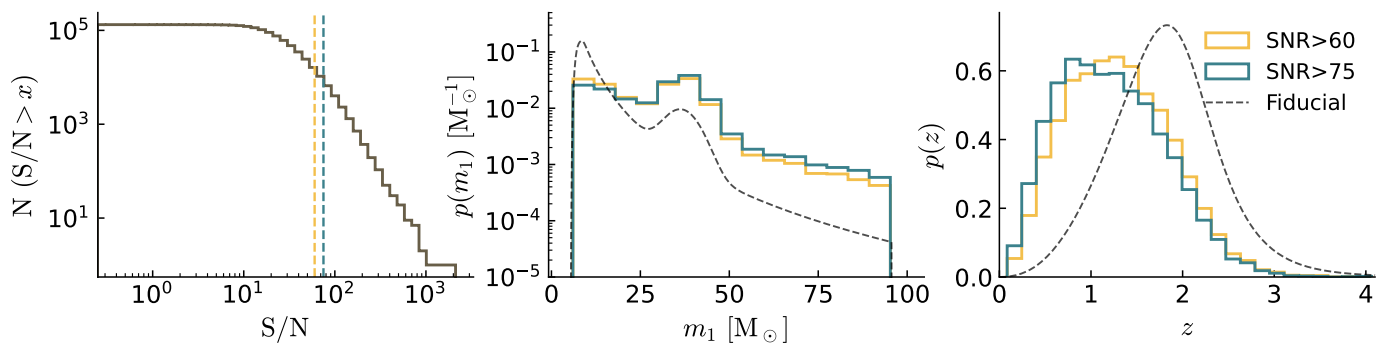


Fig. 1: Properties of the blinded mock BBH catalogs. Left panel: Reverse cumulative distribution of the S/N for the generated population. Dashed lines indicate the S/N thresholds used to define the two catalogs. Middle and right panels: mass and redshift (Eq. (13)) distributions, respectively, for events in the two catalogs, compared with the fiducial population model (dashed lines).

Using the blinded fiducial model, we first compute the total number of binary coalescences expected per detector-frame year, $\frac{dN_{\text{cbc}}}{dt_d}$. This is obtained by integrating the source-frame population rate Eq. (3) over all parameters except the coalescing time t . Then, given the drawn fiducial model, the total number of sources is:

$$\begin{aligned} \frac{dN_{\text{cbc}}}{dt_d} &= \int d\theta \frac{dN}{dt_d d\theta} = \int d\theta \frac{dN}{dt d\theta} \frac{dt}{dt_d} \\ &= R_0 \int_0^{z_{\text{max}}} dz \frac{\psi(z; \lambda_r)}{1+z} \frac{dV_c}{dz}(z; \lambda_c) \approx 1.3 \times 10^5, \end{aligned} \quad (12)$$

where z_{max} is conservatively set to 100 to cover the whole detector horizon and ensure that $\psi(x; \lambda_r) \approx 0$. In the second line of the previous equation we used the normalization of the mass distribution, and and the redshift-dependent factor $dt_d/dt = 1+z$ arising from cosmic expansion. We then randomly draw the intrinsic parameters (masses, redshifts) for each of these 1.3×10^5 sources from the fiducial population distributions. In particular, the redshift distribution, $p(z)$, describes the rate of event per unit of redshift and detector-frame time. It depends on both cosmological and merger rate parameters, and it is calculated similarly to equation Eq. (12):

$$\frac{dN_{\text{cbc}}}{dz dt_d} = \int d\bar{\theta} \frac{dN}{d\bar{\theta} dt} = R_0 \frac{\psi(z; \lambda_r)}{1+z} \frac{dV_c}{dz}(z; \lambda_c) \propto p(z) \quad (13)$$

where $\bar{\theta}$ are all event source-frame parameters except t and z . The remaining parameters describing a GW event — spin components and extrinsic parameters — are drawn from uniform distributions: the spin components are uniform in $[-1, 1]$, the inclination angle is uniform in $\cos(\iota)$ over $[0, \pi]$, the polarization angle and coalescence phase are uniformly distributed in $[0, \pi]$ and $[0, 2\pi]$, respectively, and the coalescence time — expressed in units of fraction of a day — is uniform in $[0, 1]$.

To determine which of these sources would be detected, we approximate their waveform using the IMRPhenomHM (London et al. 2018) model and we inject it into a noise realization of the detector network. For the latter, we assume a configuration of the ET made of two L-shaped 15 km long interferometers, and we consider its publicly available nominal sensitivity (Hild et al. 2011)¹. The two detectors are assumed to be located one in Sardinia and one in the Euregio Meuse-Rhine region, and are rotated by 45° with respect to each other. We then

¹ The sensitivity curve is available at <https://www.et-gw.eu/index.php/etsensitivities>

compute the signal-to-noise ratios (S/N) of each source using GWFAST (Iacovelli et al. 2022a,b).

The S/N distribution of the drawn BBHs is shown in the left panel of Fig. 1. Due to the high sensitivity of ET, the number of BBHs detected ($S/N > 8$) is 96% of the total BBH population. However, we select two sub-catalogs, one consisting of 11896 events at $S/N > 60$ and one with 6843 events at $S/N > 75$, to ease the computing load of the analysis. This dataset will then allow to extrapolate the code performances at the full expected data volume. The primary mass and redshift distributions of these two sub-catalogs are given in the central and right panel of Fig. 1.

For parameter estimation, we approximate the GW likelihood for each detected event using a Fisher information matrix (FIM) approach. This method models the posterior distribution as a multivariate Gaussian, the covariance matrix of which is the inverse of the FIM, computed with GWFAST. This approximation has been verified in previous analyses (see e.g. Borghi et al. 2024; Tagliacucchi et al. 2025), and works considered the very high S/N events considered in this study. In particular, we use emcee (Foreman-Mackey et al. 2013) to draw 5000 PE samples for each event from the multivariate Gaussian mentioned above. During the MCMC sampling we impose physical priors on GW parameters. The total prior used in each MCMC includes uniform distributions in $[0, 10^5] M_\odot$ and $[0, 1/4]$ for the chirp mass \mathcal{M}_c and the symmetric mass ratio η , respectively, while all other waveform parameters were bounded in the same physical ranges from which they were drawn. The prior on the luminosity distance is proportional to d_L^2 and bounded in $[0, 10^5]$ Gpc. The prior also includes the Jacobian of the transformation $(\mathcal{M}_c, \eta) \rightarrow (m_1^d, m_2^d)$ to ensure that the binary masses are uniformly distributed. We choose 5000 PE samples because this number is sufficient to satisfy the numerical stability criterion for the numerical integration of the integrals I_i in Eq. (1). In particular, for ICAROGW we check at each MCMC step that the number of effective samples of each event is

$$N_{\text{PE},i}^{\text{eff}} = \frac{\left(\sum_{k=0}^{N_{\text{PE}}} n_i^k \right)^2}{\sum_{j=0}^{N_{\text{PE}}} (n_i^j)^2} > 20, \quad (14)$$

where the n_i^k 's are defined in Eq. (6). For CHIMERA, instead, we check that there are enough independent weighted samples to

build the KDE by requiring

$$N_{\text{weights},i}^{\text{eff}} = \frac{\left(\sum_{k=0}^{N_{\text{PE}}} w_i^k\right)^2}{\sum_{k=0}^{N_{\text{PE}}} (w_i^k)^2} > 2, \quad (15)$$

where the w_i^k 's are given in Eq. (10) and are normalized so that they sum to 1 for each event.

Finally, to estimate the detector selection function, we perform a large-scale injection campaign, drawing 5×10^7 sources which span the whole detectable space, compute their S/N, and use the results to estimate the detection probability at each desired S/N cut. The final number of injections exceeding the S/N threshold is $\sim 4.6 \times 10^6$ and $\sim 2.7 \times 10^6$ for $\text{S/N} > 60$ and $\text{S/N} > 75$, respectively, which is sufficient to ensure the numerical stability of the Monte Carlo integral in Eq. (7). For all three codes this is (Farr 2019; Talbot & Golomb 2023; Heinzel & Vitale 2025):

$$N_{\text{inj}}^{\text{eff}} = \frac{\left[\sum_{j=0}^{N_{\text{det}}} s_j\right]^2}{\left[\sum_{j=0}^{N_{\text{det}}} s_j^2 - N_{\text{inj}}^{-1} \left(\sum_{j=0}^{N_{\text{det}}} s_j\right)^2\right]} > 5N_{\text{obs}}, \quad (16)$$

where the s_j 's are the terms in the sum over detected injections in Eq. (7).

4. Results

In this section we present the results obtained with the three pipelines and the two blinded mock BBH catalogs described in the previous section. This section is organized as follows. In Section 4.1 we analyze and compare the computational performance of the codes. In Section 4.2 we present constraints obtained from the $\text{S/N} > 75$ catalog using all three pipelines and we show the improvement achieved by lowering the S/N threshold to 60, therefore including more events. Finally, in Section 4.3 we discuss the characteristics — such as masses and redshifts — of the events producing the strongest constraints on the cosmological parameters.

To sample the likelihood implemented in CHIMERA we use the Sequential Monte Carlo sampler pocoMC (Karamanis et al. 2022a,b). For the PYMCPop-GW analyses, we employ the No-U-Turn Sampler (NUTS) within PyMC, which supports GPU sampling through the numpyro backend. The priors adopted for each hyperparameter are shown in Table 1.

4.1. Code performances

To profile the likelihoods of CHIMERA and ICAROGW, we track the time required for a single likelihood evaluation on a NVIDIA Ampere A100 GPUs with 64 GB RAM. This setup enables direct performance comparison between the two codes. The computational times are averaged over 1000 different sets of cosmological and population parameters drawn from their posterior distribution described in the following section. For the $\text{S/N} > 75$ catalog, we find that ICAROGW requires 0.093 s per likelihood evaluation, while CHIMERA requires 0.037 s, making the latter 2.5 times faster. For the $\text{S/N} > 60$ catalog, the average evaluation time becomes 0.064 s for CHIMERA and 0.14 s for ICAROGW, reducing the speed-up factor of CHIMERA to 2.2. Because PYMCPop-GW is sampled with the NUTS sampler, the relevant unit of computational

Table 1: Summary of hyperparameters and priors adopted.

Symbol	Description	Uniform prior boundaries
Cosmology (flat ΛCDM)		
H_0	Hubble constant [$\text{km s}^{-1} \text{Mpc}^{-3}$]	[20.0, 200.0]
$\Omega_{\text{m},0}$	Matter energy density	[0.01, 0.99]
Mass distribution (Power Law + Gaussian Peak)		
α	Primary power law slope	[1.5, 12]
β	Secondary power law slope	[-4, 12]
δ_m	Smoothing parameter [M_\odot]	[0.01, 10.0]
m_{low}	Power laws lower limit [M_\odot]	[2, 10]
m_{high}	Power laws upper limit [M_\odot]	[50, 200]
μ_g	Gaussian peak position [M_\odot]	[20, 50]
σ_g	Gaussian peak width [M_\odot]	[0.4, 10]
λ_g	Gaussian peak weight	[0.01, 0.99]
Rate evolution (Madau-like)		
γ	Slope at $z < z_p$	[0, 15]
κ	Slope at $z > z_p$	[0, 20]
z_p	Peak redshift	[0, 5]
R_0	Local merger rate density [$\text{Mpc}^{-3} \text{yr}^{-1}$]	[0.01, 100]

work is a Hamiltonian integration iteration, rather than a single evaluation of the likelihood. We therefore track both the wall-time per iteration and the typical number of leapfrog steps performed within each NUTS trajectory. We compile the model on GPU using the JAX/numpyro backend and run two short chains of 30 iterations to probe the performance. For the $\text{S/N} > 75$ catalog, the average cost is $\simeq 22.6$ s/it, with $N_{\text{step}} = 1023$ leapfrog steps per iteration. Therefore, the effective cost per leapfrog step is $t_{\text{step}} \simeq 22.6/1023 \simeq 0.022$ s. Since each leapfrog step requires one new evaluation of the likelihood and its gradient, this estimate provides a direct proxy for the effective ($\log \mathcal{L} + \nabla \log \mathcal{L}$) cost during sampling. For the $\text{S/N} > 60$ catalog, we obtain an average wall-time of $\simeq 30.2$ s/it, with a typical NUTS trajectory length of $N_{\text{step}} = 1023$ leapfrog steps. The effective cost in this case is therefore $t_{\text{step}} \simeq 30.2/1023 \simeq 0.03$ s per leapfrog step, i.e., per compiled ($\log \mathcal{L} + \nabla \log \mathcal{L}$) evaluation.

The population fit for the $\text{S/N} > 75$ catalog using pocoMC required approximately 6×10^5 likelihood calls and 15.5 GPU hours on a single A100 GPU for ICAROGW, while the fit with CHIMERA used $\sim 6.8 \times 10^5$ likelihood calls and about 7 GPU hours. For the $\text{S/N} > 60$ catalog, the required resources were 19 GPU hours (4.6×10^5 likelihood calls) for ICAROGW and 11.9 GPU hours (6.7×10^5 likelihood calls) for CHIMERA. The total GPU time for a NUTS MCMC run with PYMCPop-GW is computed as $t_{\text{step}} \times N_{\text{step}} \times (N_{\text{tune}} + N_{\text{draws}}) \times N_{\text{chains}}$. Here, N_{tune} is the number of steps in the warmup phase (typically 500 for simulations or 1000 for real data), and N_{draws} is the number of sampled points per chain (typically 1000 with simulations). The N_{chains} factor depends on the device: if GPU memory allows, one can vectorize the computation, reducing this factor; otherwise one has to do sequential sampling chain by chain. Assuming $N_{\text{chains}} = 4$, the MCMC fit of the $\text{S/N} > 75$ and $\text{S/N} > 60$ catalogs with PYMCPop-GW would require approximately 37.5 and 51 GPU hours, respectively.

We summarize the single-evaluation times and the convergence times in the bottom and top panels of Fig. 2, respectively. Timing results for the two analyzed catalogs are shown as points connected by a solid line.

In Fig. 2, we also forecast how the computational times for a single evaluation and for a population fit scale with the number of events and the total dataset size. These results are obtained by stacking a set of events from the $\text{S/N} > 60$ catalog until they reach a total number of events, N_{ev} , equal to 2×10^4 , 4×10^4 , and 8×10^4 . These correspond to approximate S/N cuts in our population of 47, 33, and 20, respectively. The total number of data points, D , for each case is $D = 3 \times (N_{\text{ev}} \times N_{\text{PE}} + N_{\text{inj}})$, where

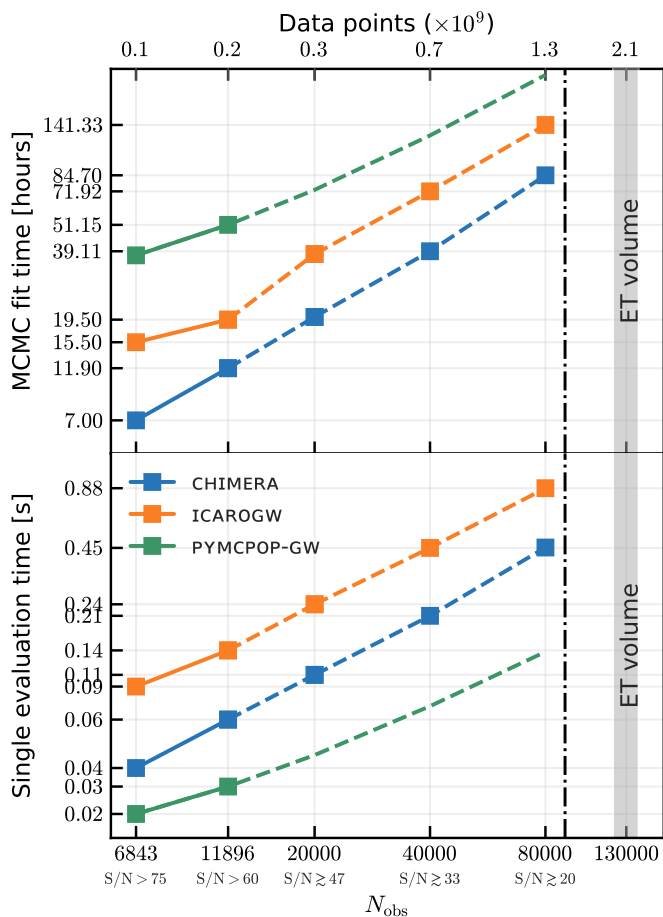


Fig. 2: Scaling of computational times for a single evaluation and for a complete population fit as a function of the number of events and the total number of data points $D = 3 \times (N_{\text{obs}} \times N_{\text{PE}} + N_{\text{inj}})$, where $N_{\text{PE}} = 5000$ per event and $N_{\text{inj}} = N_{\text{obs}} \times 390$. Markers connected by a solid line correspond to actual simulated catalogs with S/N cuts of 60 and 75, as labeled. Markers connected by a dashed line refer to timings obtained using projected catalogs constructed by stacking events and injections from the S/N > 60 catalog. The corresponding S/N cut for this number of events is indicated in the x -axis. Black vertical lines show the memory saturation limits for CHIMERA. The gray bands indicate the approximate event volume expected for ET in one year of observation.

the factor 3 represents the number of GW event parameters, i.e., the two binary masses and the luminosity distance. In each case, we consider $N_{\text{PE}} = 5000$ per event, and we scale the number of injections as $N_{\text{inj}} = N_{\text{ev}} \times 390$. The factor 390 is chosen because it matches the value present in the S/N > 60 catalog and is usually sufficient to ensure enough effective injections for the numerical stability of the Monte Carlo sum in Eq. (7). The resulting times for CHIMERA and ICAROGW are shown in Fig. 2 with markers connected by a dashed line. We observe a perfectly linear scaling with the number of events (or the total number of data points) and a constant speedup factor of 1.5–2 for CHIMERA compared to ICAROGW. On the other hand, CHIMERA saturates the RAM earlier than ICAROGW. Specifically, under our test conditions, CHIMERA cannot process more than 1×10^5 events (black vertical line in Fig. 2), while ICAROGW can handle at least the same number of events without memory issues. Overall, a single GPU can fit a

large fraction of the total volume of data predicted for ET (gray band in Fig. 2), which is about 10^5 events.

We do not forecast timings for PYMCPPOP-GW but instead plot the linear fit of the two measured points, justified by the linear scaling observed for the other codes and noted for PYMCPPOP-GW at lower event counts. The reason is that, in its current development stage, PYMCPPOP-GW is unable to produce fully converged chains on GPU for the full data volumes considered in this work. Although the method has been validated on smaller datasets ($\sim 10^3$ events), scaling it to the number of events analyzed here caused GPU memory and accuracy problems. In particular, directly materializing the full injection set for the Monte Carlo integral in Eq. (7) triggers out-of-memory errors on the GPU used in our tests. To overcome this, PYMCPPOP-GW implements a batched estimator for N_{exp} , where injections are loaded and processed in chunks of 2×10^4 injections. Despite this memory optimization, GPU sampling on the full mock catalogs still exhibits poor chain mixing after thousands of iterations. As a result, the converged PYMCPPOP-GW posterior samples presented in this paper were obtained via CPU runs. We attribute this remaining limitation to numerical aspects affecting gradient-based sampling at scale — such as interpolant resolution and the smoothing of sharp prior boundaries — which are being actively improved. Nonetheless, our tests confirm that the batched Monte Carlo strategy is fundamentally capable of supporting the data volumes expected in the ET era.

We note that all reported computation times for CHIMERA and ICAROGW were obtained using 5000 PE samples per event in each catalog. While this number is sufficient to approximate the mock GW posterior distributions obtained in this work using a FIM approach, real events may require more PE samples to accurately represent the single-event posterior, which would modify the computational times reported previously. In particular, if stricter numerical stability estimators for the likelihood Heinzel & Vitale (2025) are considered. To test this, we performed a population fit of the S/N > 60 catalog with 10000 PE samples per event using CHIMERA. With this larger catalog a single likelihood evaluation takes 0.11 s, and the complete population fit requires 22 GPU hours. This time is similar to the case with 2×10^4 events, indicating that the time scaling shown in Fig. 2 is a function of the number of data points passed to the inference.

We have demonstrated that, on a single GPU, these GPU-ready and optimized pipelines can process up to 10^5 events — with up to 10^4 PE samples per event — and 2.7×10^6 injections in about one or two weeks of dedicated computing time. Since the likelihood in Eq. (1) is perfectly parallelizable over events — meaning the single event contribution to the likelihood can be computed independently and combined at the end — the optimal strategy for the ET era is to exploit this property by distributing the workload across multiple GPUs. This can be achieved using well-established protocols such as the Message Passing Interface (MPI) or through new JAX sharding features (Bradbury et al. 2018). By splitting the dataset across few GPUs, a number already accessible at current HPC facilities, pipelines can easily scale to handle the volume of data of the ET. However, we warrant that more complex astrophysical models or the requirement of stricter numerical stability estimators might require more memory. Such a demand may be prohibitive for the expected volume of GW detections from ET. Therefore, further computational improvements to ICAROGW, PYMCPPOP-GW, and CHIMERA may be necessary.

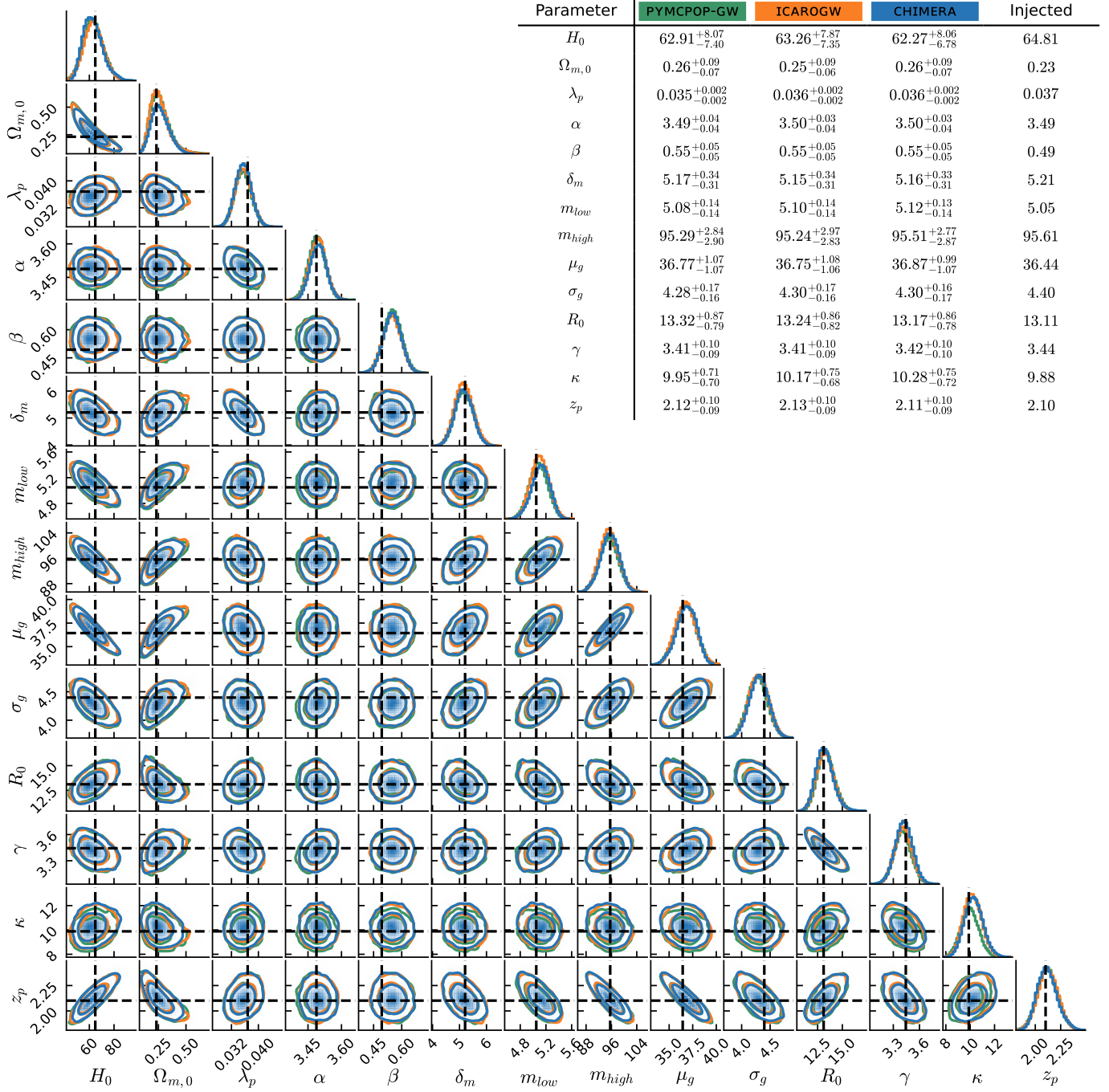


Fig. 3: Cosmological and population parameter constraints from the $S/N > 75$ catalog. The corner plot shows 1D marginalized posteriors and 2D contours (68% and 95% credible regions) obtained with all three pipelines. The inset table provides median values and 68% C.I. for each parameter.

4.2. Constraints

Figure 3 presents a corner plot showing the 1D marginalized posterior distributions and 2D marginalized contours at the 68% and 95% credible regions for all population and cosmological parameters. The inset table summarizes the median values and 68% credible intervals (C.I.) for each parameter as obtained by all three codes.

The constraints from all three pipelines are in excellent agreement; each recovers fully compatible contours, exhibiting the same correlation patterns among cosmological and population

parameters. All three codes recover nearly every fiducial cosmological and population parameter within the 68% C.I., and every parameter within the 95% C.I. Thanks to the depth and size of the ET catalog, we can reveal for the first time correlations between the cosmological parameters H_0 , $\Omega_{m,0}$ and the population parameters, which were not observed in studies currently available. For example, we find that the cosmological parameters correlate with all the population parameters related to mass features, while in current constraints the only correlation that we can observe is the one with the location of two mass features at $\sim 10M_\odot$ and $\sim 30M_\odot$ in the BBH mass spectrum (Abac et al. 2025b). We

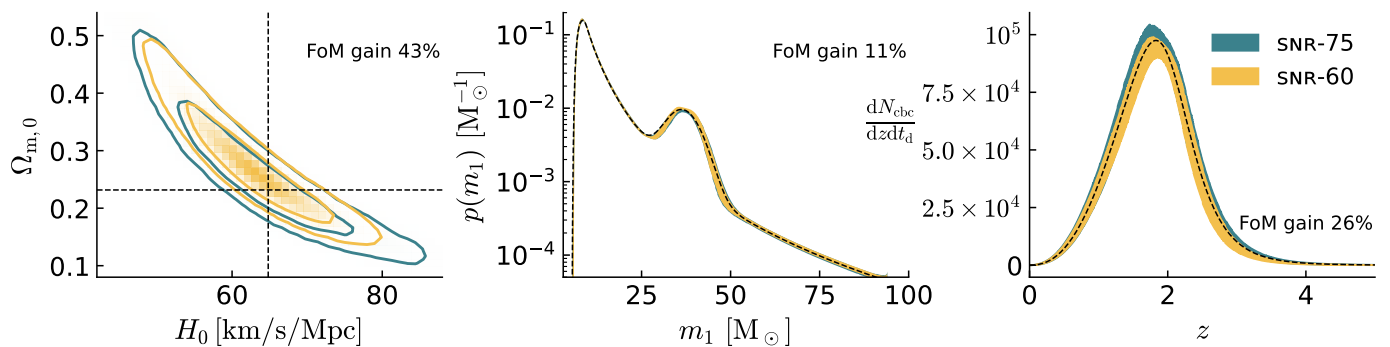


Fig. 4: Comparison of constraints from the $S/N > 60$ and $S/N > 75$ catalogs. Left: 2D marginalized posterior for $(H_0, \Omega_{m,0})$. In particular, we plot the 68% and 95% credible regions. Center and right: predictive posterior distributions for the primary mass spectrum and the redshift event rate Eq. (13), respectively. Dashed lines indicate the blinded fiducial values and population model.

also note that because the catalog extends to redshifts beyond the Madau–Dickinson peak, z_p , we can measure z_p directly, rather than placing lower bounds as done with current redshift-limited data. This is also of crucial importance for dark siren cosmology, as the position of z_p provides another population-level redshift scale that can be used to infer cosmology (Ye & Fishbach 2021). This demonstrates the importance of the ET for constraining and understanding the population of BBHs, particularly at high redshift.

A central physical problem beyond the scope of this work, which instead focuses more on the analyses feasibility, is the impact that a redshift-evolving BBH distribution would have on the cosmological inference. Recent studies (Mukherjee 2022; Karathanasis et al. 2023; Pierra et al. 2024; Agarwal et al. 2025) argue that a redshift evolution of the mass spectrum could already bias the cosmological parameters inference for current-generation GW events. Possible mechanisms that could source redshift evolution in the mass spectrum — or contaminate it in general — include contributions from multiple formation channels (Wong et al. 2021; Zevin & Holz 2022; Tornamenti et al. 2024; Fishbach 2025), Population III star mergers (Woosley & Heger 2021; van Son et al. 2022), mergers in dense stellar cluster (Antonini & Rasio 2016; Mapelli et al. 2022; Gerosa & Fishbach 2021; Ye & Fishbach 2024), or mergers in AGN accretion disks (Ford & McKernan 2022). This problem will be even more important for ET, given its extended redshift range. A viable approach to incorporating redshift evolution in the mass spectrum without biasing cosmological analyses may rely on the use on non-parametric models, such as the ones proposed in Rinaldi et al. (2024); Heinzl et al. (2025); Farah et al. (2025); Sadiq et al. (2025).

To assess how the inclusion of lower S/N events affects the inference, we compare the constraints obtained from the $S/N > 60$ and $S/N > 75$ catalogs. This comparison is performed by combining the samples obtained from the three different pipelines for each catalog. Figure 4 presents this comparison across three different metrics: the joint constraints on the Hubble constant and matter density parameter $(H_0, \Omega_{m,0})$; the predictive posterior distribution of the primary mass spectrum $p(m_1)$; and the event rate distribution per unit redshift and detector-frame time Eq. (13). To quantify the improvement in these three metrics, we also compute their Figure of Merit (FoM), defined as the inverse of the area of the 68% credible region. The improvement factors — reported as insets in Fig. 4 — are significant for all three metrics. Whereas the improvements in the H_0 - $\Omega_{m,0}$ constraints and in the rate distribution $\frac{dN_{\text{ebc}}}{dz dt_d}$ are visually apparent in the figure,

the FoM is essential for assessing the improvement in the mass distribution. In fact, the two reconstructed curves for $p(m_1)$ are very similar, as both are precise and close to the fiducial distribution.

We find a joint precision of 12% on H_0 and 31% on $\Omega_{m,0}$ for the $S/N > 75$ catalog, which contains 6843 BBHs. Although the $S/N > 60$ catalog includes approximately twice the number of events, the constraints on H_0 and $\Omega_{m,0}$ remain at the 10.5% and 26% level, respectively. The improvement is consistent with a $\sim \sqrt{2}$ improvement given by the increased number of GW events considered in the analysis. Besides the parameters of the distance–redshift relation, spectral sirens can yield a valuable constraint on the Hubble function $H(z)$ at intermediate redshifts, provided a Λ CDM evolution is assumed (Farr 2019; Mancarella et al. 2022; Farah et al. 2025). To prove this, we compute $H(z)/(1+z)$ on a redshift grid for each sample of H_0 and $\Omega_{m,0}$, thereby obtaining samples that represent the posterior predictive distribution of $H(z)/(1+z)$. From this distribution, we then calculate the median and the 68% C.I. Figure 5 shows such constraint (top), together with the relative precision (bottom). For the $S/N > 75$ and $S/N > 60$ catalogs, we find that the best constraints on $H(z)$ are achieved at redshifts $z \approx 1.41$ and $z \approx 1.53$ (vertical dashed lines in the bottom panel of Fig. 5), with corresponding precisions of 3.04% and 2.37%, respectively. Interestingly, the redshift range where we get the best constraints on $H(z)$ is close to the one typically used to constrain the transition redshift of the Universe’s expansion history (Moresco et al. 2016). For example, in the $0.7 < z < 1.8$ interval, the mean precisions on $H(z)$ are 3.5% ($S/N > 75$) and 2.8% ($S/N > 60$). Having the tightest spectral siren constraints in this interval is promising, since estimates of $H(z)$ in this range usually rely on not fully cosmology-independent cosmological probes. Note, however, that the strength of the constraint might depend on assumptions on the fiducial cosmological model (Pierra et al. 2025).

These findings differ from those of Califano et al. (2025), who reported a $\sim 6\%$ measurement on both parameters using only 1659 events above $S/N > 80$ (though assuming the ET in a triangular configuration). This difference is also notable because the predictive posterior distributions of the mass and redshift rate distributions shown in Fig. 4 are considerably tighter than those presented by such analysis, as would be expected given our significantly larger event sample. Additionally, our analysis reveals a distinct set of correlations between cosmological and population parameters that were not identified in previous studies (Califano et al. 2025). Further, we also mention that Chen et al.

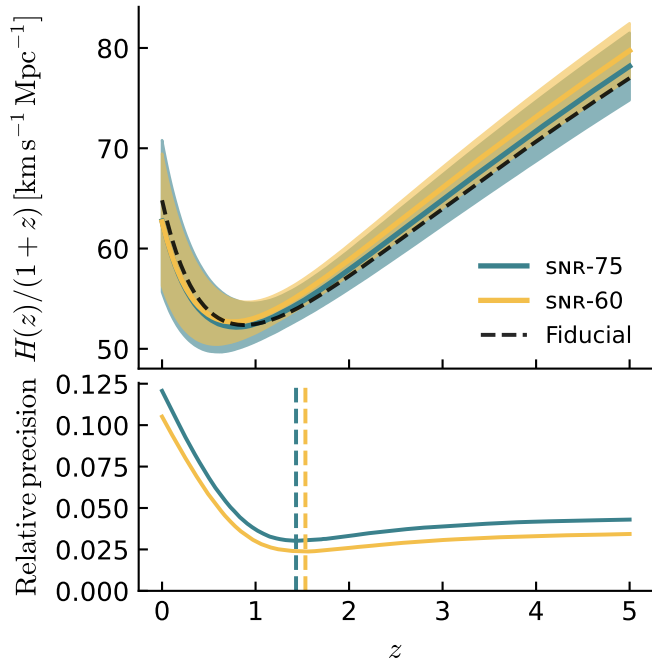


Fig. 5: Top: The $1\text{-}\sigma$ contours of the predictive posterior distribution for $H(z)/(1+z)$. Bottom: The relative precision on $H(z)$, computed as the width of the $1\text{-}\sigma$ C.I. divided by twice the median of $H(z)$. Dashed vertical lines indicate the redshift at which the constraint on $H(z)$ is strongest.

(2024) found that with 3G detectors it will be possible to achieve percent-level constraints on the Hubble constant and $\Omega_{m,0}$ using 5×10^4 events. Rescaling our result to the same number of events using the expected statistical scaling $1/\sqrt{N}$ yields an uncertainty of order $\sim 4\%$. From Fig. 6 of Chen et al. (2024), one can infer an uncertainty of about 2% on H_0 , which is broadly comparable once the methodological and modeling differences between the two analyses are taken into account.² Two aspects are particularly worth noting. First, single-event error estimates in Chen et al. (2024) are calibrated on simulations of CE performed several years ago (Vitale & Evans 2017), and sensitivity curves are known to evolve over time as detector designs are updated. Second, their population model includes binary neutron star systems, which provide an additional and important mass scale that strengthens constraints (Ezquiaga & Holz 2022). Overall, these considerations suggest that achieving percent-level constraints on H_0 with spectral sirens is possible with (1) as large a number of events as possible, rather than restricting the analysis to only high-S/N detections, and (2) the inclusion of as many mass scales as possible in the observed population. A further conclusion, consistent with previous work, is that the strongest constraints from spectral sirens are not obtained on H_0 , but rather on the expansion rate $H(z)$ at intermediate redshifts. Interestingly, our findings suggest that this is possible even with a smaller sample of high-S/N events (see Fig. 5).

While the tighter constraints on H_0 , $\Omega_{m,0}$ reported by earlier works may be due to the use of population models with sharper features than the blind one adopted in this study (e.g., in Califano et al. 2025; Chen et al. 2024), or to the larger dataset considered (Chen et al. 2024), this comparison underscores the

² Also note that the $1/\sqrt{N}$ scaling does not account for the different S/N cut in the two analyses.

need for fiducial forecasts in the era of the ET and third-generation detectors. Such forecasts should be based on realistic catalogs generated beyond the Fisher-matrix approximation and should incorporate updated population models and sensitivity curves to properly assess the cosmological potential of ET using spectral sirens. As this detailed forecast study was beyond the scope of the present work, we defer it to future investigations. If the results found in this work will reveal true, achieving constraints on H_0 comparable to those from the Cosmic Microwave Background and supernovae with just high-S/N events from 3G detectors may require the complementary use of galaxy catalogs, sharper features in the population model (Abac et al. 2025c; Tiwari 2025; Pierra & Papadopoulos 2026; Tagliacruzchi et al. 2026), or additional information on $\Omega_{m,0}$ that can be obtained from other probes such as Baryonic Acoustic Oscillations (Adame et al. 2025) or uncalibrated Supernovae measures (Riess et al. 2022). In fact, fixing $\Omega_{m,0}$ to its fiducial value improves the constraint on H_0 to 3% using the S/N > 75 catalog, corresponding to a factor $4\times$ of improvement over the case where $\Omega_{m,0}$ is marginalized over (see Section A). Otherwise, the inclusion of a larger sample of spectral sirens can be envisaged, with the corresponding accurate treatment of selection effects. A valuable constraint on $H(z)$ at intermediate redshifts seems a concrete possibility in all cases.

4.3. Constraining power

We assess which events contribute most significantly to constraining cosmological parameters and population hyperparameters, focusing specifically on H_0 , $\Omega_{m,0}$, and μ_g . To quantify each event's contribution, we compute Pearson correlation coefficients, $\rho_{i,\lambda}$, between the marginal likelihood of the i -th event and the aforementioned hyperparameters. The i -th event marginal likelihood is the single-event contribution to the total hyperlikelihood Eq. (1), i.e.,

$$\log \mathcal{L}_i(d_i | \Lambda) \propto \log \left(\int d\theta_{d,i} \mathcal{L}_{\text{gw}}(d_i | \theta_{d,i}) \left| \frac{d\theta_i}{d\theta_{d,i}} \right| \frac{dN}{d\theta_i}(\Lambda) \right) - \frac{N_{\text{exp}}(\Lambda)}{N_{\text{obs}}}. \quad (17)$$

The resulting coefficients are shown in Fig. 6, where we show the 2D histogram of the mock GW events with S/N > 75 in the $m_{d,1}$ - d_L plane. The color of each (30×30) logarithmically-spaced bin represents the mean Pearson correlation coefficient calculated from the events falling within that bin. The curves overlaid on each panel correspond to $m_{d,1} \cdot p(m_1(m_{d,1}, d_L, \lambda_c) | \lambda_m)$ at different values of H_0 (but with λ_m fixed to the fiducial) and at various luminosity-distance levels. In particular, we plot these curves for $d_L = 1, 2, 6, \text{ and } 16$ Gpc, corresponding to $z = 0.19, 0.34, 0.84, \text{ and } 1.83$ given the fiducial $H_0 \approx 64.8 \text{ km s}^{-1} \text{ Mpc}^{-3}$.

Events with highest Pearson coefficients are those that constrain the considered hyperparameters most strongly. For H_0 , $\Omega_{m,0}$, and μ_g these are found at low luminosity distances ($d_L < 2$ Gpc) and around the structures of the mass spectrum, while for γ they are distributed across the whole parameter space. In particular, events with masses lower than the Gaussian peak are negatively correlated with μ_g , whereas those with masses higher than the peak are positively correlated. This means that events below and above the peak pull μ_g toward lower and higher values, respectively, with the final constraint set by the balance of these two effects. Similarly, constraints on H_0 and $\Omega_{m,0}$ are driven mainly by events near the low-mass edge (m_{low}) and around the Gaussian peak. For H_0 , the correlation signs near the

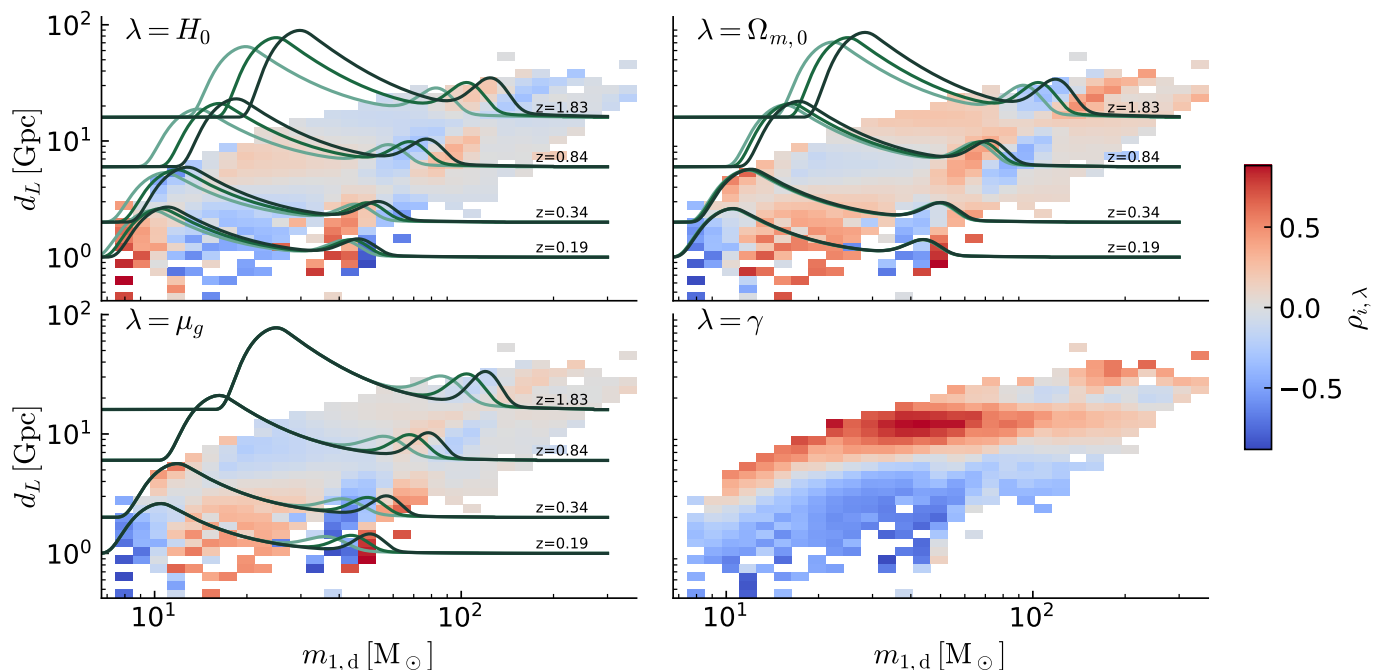


Fig. 6: 2D histogram of the events with $S/N > 75$ in the d_L - $m_{1,d}$ plane. Color indicates the mean Pearson correlation coefficient between the marginal likelihood of events in each bin and the hyperparameters H_0 (top left), $\Omega_{m,0}$ (top right), μ_g (bottom left), and γ (bottom right). In each panel we plot the function $m_{1,d} \cdot p(m_{1,d})$ for different values of the hyperparameter considered and at various luminosity-distance levels. In particular, such curves are calculate d for (from light to dark green): $H_0 \in [40, 64.8, 90] \text{ km s}^{-1} \text{ Mpc}^{-1}$, $\Omega_{m,0} \in [0.05, 0.23, 0.55]$, and $\mu_g \in [30, 36.44, 42] \text{ M}_\odot$. The redshifts corresponding to the distances considered (calculated with the fiducial $H_0 \approx 64.8 \text{ km s}^{-1} \text{ Mpc}^{-1}$) are also indicated.

peak are opposite to those for μ_g , consistent with the H_0 - μ_g anticorrelation visible in Fig. 3. The physical origin of this anticorrelation is that a higher H_0 increases the redshift corresponding to a fixed d_L , which in turn requires a smaller inferred μ_g to match the observed data. The correlation-sign pattern for $\Omega_{m,0}$ is opposite to that for H_0 , reflecting their mutual anticorrelation (see Fig. 4).

Regarding γ , low-distance events tend to reduce its value, while events with $d_L > 6 \text{ Gpc}$ — corresponding to $z \approx 0.84$ in the fiducial cosmology, near the peak in the observed redshift distribution Fig. 1 — favor higher value of γ . Moreover, around this luminosity distance value the correlation-sign pattern for H_0 , $\Omega_{m,0}$, and μ_g reverses. This occurs because at these redshifts events constrain mainly $\Omega_{m,0}$ rather than H_0 : the Pearson coefficients relative to H_0 and μ_g become smaller, whereas those relative $\Omega_{m,0}$ remain relevant. Since H_0 and $\Omega_{m,0}$ are anticorrelated, the sign pattern for the three hyperparameters flips. To verify this, we compute the Pearson coefficients between events and H_0 , μ_g , and γ while fixing $\Omega_{m,0}$ to its fiducial value. The resulting coefficients, shown in Section A, confirm that the sign reversal does not occur in that case at this distance.

At even greater distances — around $d_L \approx 16 \text{ Gpc}$ ($z \approx 1.83$) — events primarily constrain $\Omega_{m,0}$ and γ . Furthermore, the correlation-sign pattern for H_0 , $\Omega_{m,0}$, and μ_g reverts once more to that seen at lower luminosity distances. This second transition occurs because, at this distance, the correlation of events — that lie near the peak of the true redshift distribution — with γ changes sign. Since γ itself is correlated with $\Omega_{m,0}$, μ_g and anticorrelated with H_0 , the change in how events influence γ propagates and reverses the sign patterns for the other hyperparameters. This interpretation is supported by the case in which $\Omega_{m,0}$

is fixed (see Section A), where the same transition is seen at the same luminosity distance.

5. Conclusion

In this work, we performed a blinded mock data challenge to test current spectral siren cosmological inference pipelines for the high-statistics regime of 3G interferometers. We focused on assessing the computational scalability, the agreement between independent code implementations, and the constraining power for cosmology expected from an observatory like the ET. Our study yields several key conclusions.

First, we demonstrated that GPU-accelerated pipelines, such as ICAROGW, CHIMERA, and PYMCPOP-GW, can handle the large data volume expected from third-generation detectors. By profiling their performance, we found that these codes can process up to $\sim 8 \times 10^4$ – 10^5 events with thousands of posterior samples PE samples each on a single GPU within a manageable timeframe, confirming that GPU acceleration is the key for cosmological analyses in the third-generation era. Second, through a blinded comparison, we validated that three independent implementations of the spectral siren likelihood produce fully consistent cosmological and population parameter constraints, confirming the robustness of the method. Third, we forecast joint cosmological and population parameters constraints from the blinded population model, finding a 2.37% constraint on the Universe’s expansion history $H(z)$ at $z \approx 1.53$ using 11896 events detected at high S/N by the ET. This corresponds to joint constraints of 10.5% on H_0 and 26.5% on $\Omega_{m,0}$. Moreover, the mean precisions on $H(z)$ in the $0.7 < z < 1.8$ range are 3.5% for the $S/N > 75$ catalog and 2.8% for the $S/N > 60$ one. Finally, we identified the

specific events that drive cosmological constraints, revealing distinct correlation patterns between hyperparameters and features in the $m_{d,1} - d_L$ distribution of events. In particular, we found that low distance events constrain well all cosmological parameters, while at larger distances the events constrain mainly $\Omega_{m,0}$.

Looking ahead, several important directions emerge from this study. While GPU acceleration already enables the analysis of a large fraction of events that will be detected by the ET, analyzing future catalogs entirely will require the pipelines to evolve further. Key developments include advanced parallelization strategies using distributed GPU computing and efficient GPU memory handling. Our analysis assumed a simple, non-evolving population model with randomly chosen fiducial hyperparameters. Future work must incorporate more realistic astrophysics to provide more robust cosmological constraints. Since ET will detect events at higher redshifts, and since spectral sirens can be combined with galaxy catalogs or additional probes (e.g., BAO) to increase their constraining power, future cosmological forecast should include also the evolving dark energy equation of state.

Nevertheless, our results confirm the feasibility of spectral siren cosmology with a large number of events, providing a validated, performance-tested framework that paves the way for precision cosmology with third-generation GW observatories.

Acknowledgements. We acknowledge the ICSC for awarding this project access to the EuroHPC supercomputer LEONARDO, hosted by CINECA (Italy). M.T. acknowledges the funding from the European Union - NextGenerationEU, in the framework of the HPC project – “National Center for HPC, Big Data and Quantum Computing” (PNRR - M4C2 - I1.4 - CN00000013 – CUP J33C22001170001). M.Mo. acknowledges the financial contribution from the grant PRIN-MUR 2022 2022NY2ZRS 001 “Optimizing the extraction of cosmological information from Large Scale Structure analysis in view of the next large spectroscopic surveys”. M.Mo. and N.B. acknowledge support from the grant ASI n. 2024-10-HH.0 “Attività scientifiche per la missione Euclid – fase E”. The work of M.Ma. and A.A. is supported by the French government under the France 2030 investment plan, as part of the Initiative d’Excellence d’Aix-Marseille Université – A*MIDEX AMX-22-CEI-02. S.M. is supported by ERC grant GravitySirens 101163912. Funded by the European Union. Views and opinions expressed are however those of the author(s) only and do not necessarily reflect those of the European Union or the European Research Council Executive Agency. Neither the European Union nor the granting authority can be held responsible for them. S.F. work received support from the French government under the France 2030 investment plan, as part of the Excellence Initiative of Aix Marseille University - amidex (AMX-19-IET-008 -IPhU).

References

Abac, A. et al. 2025a, [arXiv: 2503.12263]
 Abac, A. G. et al. 2025b, [arXiv: 2509.04348]
 Abac, A. G. et al. 2025c, [arXiv: 2508.18083]
 Abac, A. G. et al. 2025d, [arXiv: 2508.18082]
 Abbott, B., Abbott, R., Abbott, T., & Abernathy, M. 2016, *Physical Review Letters*, 116
 Abbott, B. P., Abbott, R., Abbott, T. D., et al. 2019, *Phys. Rev. X*, 9, 031040
 Abbott, B. P., Abbott, R., Abbott, T. D., et al. 2021a, *The Astrophysical Journal*, 909, 218
 Abbott, R., Abbott, T. D., Abraham, S., et al. 2021b, *Phys. Rev. X*, 11, 021053
 Abbott, R., Abbott, T. D., Acernese, F., et al. 2023a, *Phys. Rev. X*, 13, 041039
 Abbott, R., Abe, H., Acernese, F., et al. 2023b, *The Astrophysical Journal*, 949, 76
 Abbott, R. et al. 2021c, *Astrophys. J. Lett.*, 913, L7
 Abbott, R. et al. 2023c, *ApJ*, 949, 76
 Adame, A. G. et al. 2025, *JCAP*, 02, 021
 Agarwal, A. et al. 2025, *Astrophys. J.*, 987, 47
 Antonini, F. & Rasio, F. A. 2016, *Astrophys. J.*, 831, 187
 Belfiglio, A., Luongo, O., & Mancini, S. 2022, *Phys. Rev. D*, 105, 123523
 Borghi, N., Mancarella, M., Moresco, M., et al. 2024, *ApJ*, 964, 191
 Bradbury, J., Frostig, R., Hawkins, P., et al. 2018, <http://github.com/jax-ml/jax>
 Branchesi, M. et al. 2023, *JCAP*, 07, 068
 Califano, M., De Martino, I., & Vernieri, D. 2025, *Phys. Rev. D*, 111, 123535

Chen, H.-Y., Ezquiaga, J. M., & Gupta, I. 2024, *CQG*, 41, 125004
 Chen, H.-Y., Fishbach, M., & Holz, D. E. 2018, *Nature*, 562, 545–547
 Del Pozzo, W. 2012, *Physical Review D*, 86
 Evans, M. et al. 2021, [arXiv: 2109.09882]
 Ezquiaga, J. M. & Holz, D. E. 2022, *PRL*, 129, 061102
 Farah, A. M., Callister, T. A., Ezquiaga, J. M., Zevin, M., & Holz, D. E. 2025, *ApJ*, 978, 153
 Farr, W. M. 2019, *Research Notes of the AAS*, 3, 66
 Finke, A., Foffa, S., Iacovelli, F., Maggiore, M., & Mancarella, M. 2021, *JCAP*, 2021, 026
 Fishbach, M. 2025, *Class. Quant. Grav.*, 42, 055009
 Fishbach, M., Gray, R., & Hernandez, I. M. 2019, *ApJL*, 871, L13
 Ford, K. E. S. & McKernan, B. 2022, *Mon. Not. Roy. Astron. Soc.*, 517, 5827
 Foreman-Mackey, D., Hogg, D. W., Lang, D., & Goodman, J. 2013, *Publ. Astron. Soc. Pac.*, 125, 306
 Gair, J. R., Ghosh, A., Gray, R., et al. 2023, *ApJ*, 166, 22
 Gerosa, D. & Fishbach, M. 2021, *Nature Astron.*, 5, 749
 Gray, R., Hernandez, I. M., Qi, H., et al. 2020, *Phys. Rev. D*, 101
 Gray, R., Messenger, C., & Veitch, J. 2022, *MNRAS*, 512, 1127
 Gray, R. et al. 2023, *JCAP*, 12, 023
 Heinzl, J., Mould, M., & Vitale, S. 2025, *Phys. Rev. D*, 111, L061305
 Heinzl, J. & Vitale, S. 2025, [arXiv: 2509.07221]
 Hild, S. et al. 2011, *CQG*, 28, 094013
 Holz, D. E. & Hughes, S. A. 2005, *The Astrophysical Journal*, 629, 15–22
 Iacovelli, F., Mancarella, M., Foffa, S., & Maggiore, M. 2022a, *ApJ*, 941, 208
 Iacovelli, F., Mancarella, M., Foffa, S., & Maggiore, M. 2022b, *ApJ. Supp.*, 263, 2
 Jin, S.-J., Song, J.-Y., Sun, T.-Y., et al. 2026, *Sci. China Phys. Mech. Astron.*, 69, 220401
 Karamanis, M., Beutler, F., Peacock, J. A., Nabergoj, D., & Seljak, U. 2022a, *MNRAS*, 516, 1644
 Karamanis, M., Nabergoj, D., Beutler, F., Peacock, J. A., & Seljak, U. 2022b, *J. Open Source Softw.*, 7, 4634
 Karathanasis, C., Mukherjee, S., & Mastrogiovanni, S. 2023, *Mon. Not. Roy. Astron. Soc.*, 523, 4539
 London, L., Khan, S., Fauchon-Jones, E., et al. 2018, *PRL*, 120, 161102
 Madau, P. & Dickinson, M. 2014, *Ann. Rev. Astron. Astrophys.*, 52, 415
 Maggiore, M., Broeck, C. V. D., Bartolo, N., et al. 2020, *JCAP*, 2020, 050–050
 Mancarella, M., Genoud-Prachex, E., & Maggiore, M. 2022, *PRD*, 105, 064030
 Mancarella, M. & Gerosa, D. 2025, *Phys. Rev. D*, 111, 103012
 Mandel, I., Farr, W. M., & Gair, J. R. 2019, *MNRAS*, 486, 1086
 Mapelli, M., Bouffanoy, Y., Santoliquido, F., Sedda, M. A., & Artale, M. C. 2022, *Mon. Not. Roy. Astron. Soc.*, 511, 5797
 Mastrogiovanni, S., Laghi, D., Gray, R., et al. 2023, *PRD*, 108, 042002
 Mastrogiovanni, S., Leyde, K., Karathanasis, C., et al. 2021, *Phys. Rev. D*, 104
 Mastrogiovanni, S., Pierra, G., Perriès, S., et al. 2024, *A&A*, 682, A167
 Moresco, M., Pozzetti, L., Cimatti, A., et al. 2016, *JCAP*, 05, 014
 Moresco, M. et al. 2022, *Living Rev. Relativ.*, 25, 6
 Mukherjee, S. 2022, *Mon. Not. Roy. Astron. Soc.*, 515, 5495
 Pierra, G., Colombo, A., & Mastrogiovanni, S. 2025, [arXiv: 2511.11795]
 Pierra, G., Mastrogiovanni, S., Perriès, S., & Mapelli, M. 2024, *PRD*, 109, 083504
 Pierra, G. & Papadopoulos, A. 2026, [arXiv: 2601.03257]
 Punturo, M., Abernathy, M., Acernese, F., et al. 2010, *CQG*, 27, 194002
 Reitze, D. et al. 2019, *Bull. Am. Astron. Soc.*, 51, 035
 Riess, A. G. et al. 2022, *Astrophys. J. Lett.*, 934, L7
 Rinaldi, S., Del Pozzo, W., Mapelli, M., Lorenzo-Medina, A., & Dent, T. 2024, *Astron. Astrophys.*, 684, A204
 Sadiq, J., Dent, T., & Lorenzo-Medina, A. 2025, *Phys. Rev. D*, 112, 083028
 Schutz, B. F. 1986, *Nature*, 323, 310
 Tagliazucchi, M., Moresco, M., Borghi, N., & Ciapetti, C. 2026, [arXiv: 2601.03347]
 Tagliazucchi, M., Moresco, M., Borghi, N., & Fiebig, M. 2025, *A&A*, 702, A244
 Talbot, C. & Golomb, J. 2023, *MNRAS*, 526, 3495
 Taylor, S. R., Gair, J. R., & Mandel, I. 2012, *PRD*, 85, 023535
 Tiwari, V. 2018, *Class. Quant. Grav.*, 35, 145009
 Tiwari, V. 2025, [arXiv: 2510.25579]
 Torniamanti, S., Mapelli, M., Périgois, C., et al. 2024, *Astron. Astrophys.*, 688, A148
 van Son, L. A. C., de Mink, S. E., Callister, T., et al. 2022, *Astrophys. J.*, 931, 17
 Vitale, S. & Evans, M. 2017, *Phys. Rev. D*, 95, 064052
 Vitale, S., Gerosa, D., Farr, W. M., & Taylor, S. R. 2020, in *Handbook of Gravitational Wave Astronomy*
 Wong, K. W. K., Breivik, K., Kremer, K., & Callister, T. 2021, *Phys. Rev. D*, 103, 083021
 Woosley, S. E. & Heger, A. 2021, *Astrophys. J. Lett.*, 912, L31
 Ye, C. & Fishbach, M. 2021, *Phys. Rev. D*, 104, 043507
 Ye, C. S. & Fishbach, M. 2024, *Astrophys. J.*, 967, 62
 Zevin, M. & Holz, D. E. 2022, *Astrophys. J. Lett.*, 935, L20

Appendix A: Results with $\Omega_{m,0}$ fixed

In this appendix, we present and discuss the results obtained under the assumption that $\Omega_{m,0}$ is held fixed at its fiducial value.

In Fig. A.1, we compare the constraints derived from the $S/N > 75$ catalog under two assumptions: one where $\Omega_{m,0}$ is fixed to its fiducial value, and another where it is marginalized over. The figure shows only the parameters most correlated with $\Omega_{m,0}$ because the marginalized 1D posteriors for the other parameters remain nearly unchanged. Fixing $\Omega_{m,0}$ significantly improves the precision of the following parameters:

- H_0 : uncertainty improves from 12% to 3%.
- μ_g : uncertainty improves from 2.8% to 1.4%.
- z_p : uncertainty improves from 4.5% to 2.8%.
- m_{low} : uncertainty improves from 2.6% to 1.77%.
- m_{high} : uncertainty improves from 2.95% to 1.85%.

In Fig. A.2 we show the Pearson correlation coefficients between individual events and the hyperparameters H_0 , μ_g , and γ , similarly to the results shown in Fig. 6. We note that:

- The first sign reversal, observed in Fig. 6 in the full parameter analysis at $d_L \sim 6$ Gpc ($z \approx 0.84$), does not occur here. This absence confirms that such reversal is a direct consequence of the anticorrelation between H_0 and $\Omega_{m,0}$.
- The second sign reversal, observed at $d_L \sim 16$ Gpc ($z \approx 1.83$), is still present even with $\Omega_{m,0}$ fixed. This confirms that the mechanism driving this high-distance reversal is due to originates from the changing relationship between distant events and γ .

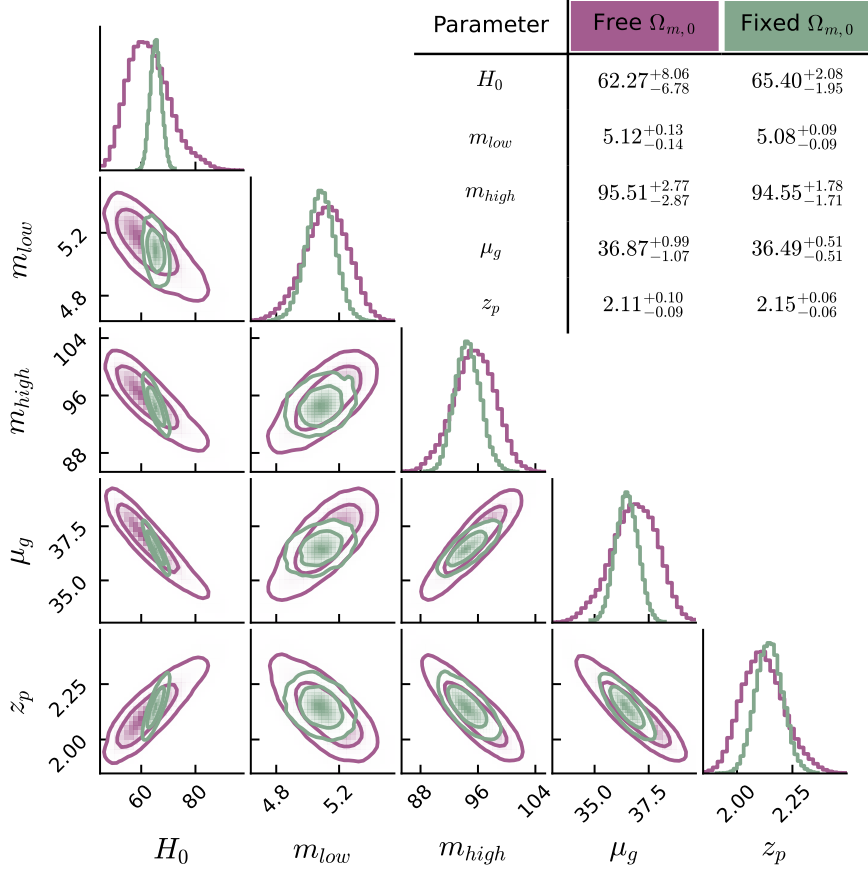


Fig. A.1: Comparison of the constraints obtained from the $S/N > 75$ catalog when the matter density parameter $\Omega_{m,0}$ is fixed to its fiducial value (green) and when it is marginalized over (purple). Only parameters significantly correlated with H_0 are shown.

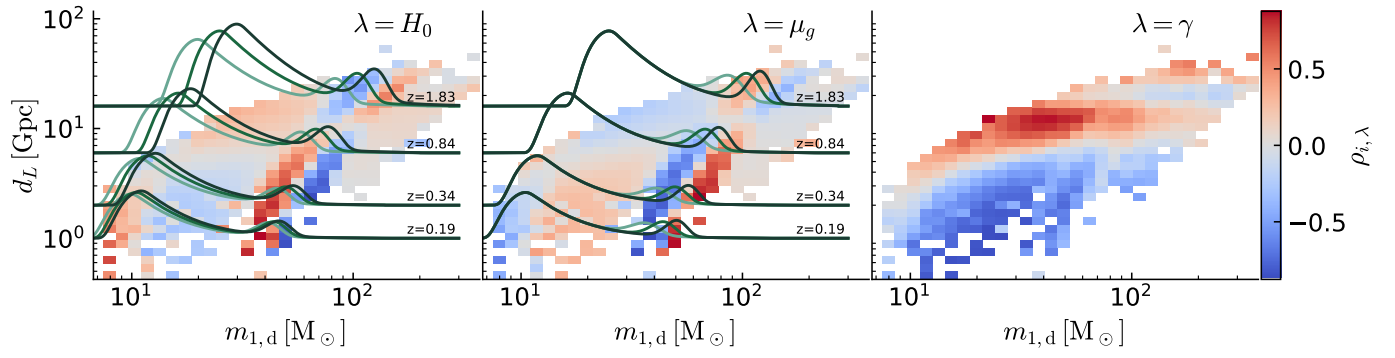


Fig. A.2: Pearson correlation coefficients between events and hyperparameters, with $\Omega_{m,0}$ fixed. Only the high-distance ($d_L \sim 16$ Gpc) sign reversal is present, while the reversal at $d_L \sim 6$ Gpc disappears.